Surface-to-space atmospheric waves from Hunga Tonga-Hunga Ha'apai eruption

Corwin J Wright*[1], Neil P Hindley[1], M Joan Alexander[2], Mathew Barlow[3], Lars Hoffmann[4], Cathryn N Mitchell[1], Fred Prata[5,6], Marie Bouillon[7], Justin Carstens[8], Cathy Clerbaux[7], Scott M Osprey[9], Nick Powell[10], Cora E Randall[11,12], and Jia Yue[13,14]

1. Centre for Space, Atmospheric and Oceanic Science, University of Bath, Bath, UK
2. Northwest Research Associates, Boulder, Colorado, USA
3. Environmental, Earth & Atmospheric Sciences, University of Massachusetts Lowell, Massachusetts, USA
4. Jülich Supercomputing Center, Forschungszentrum Jülich, Jülich, Germany
5. AIRES, Mt Eliza, Victoria, Australia
6. School of Electrical Engineering, Computing & Mathematical Science, Curtis University, Western Australia
7. LATMOS/IPSL, Sorbonne Université/UVSQ/CNRS, Paris, France
8. Center for Space Science and Engineering Research, Bradley Department of Electrical and Computer Engineering, Virginia Tech, Blacksburg, VA, USA
9. Atmospheric, Oceanic and Planetary Physics, Department of Physics, University of Oxford, Oxford, UK
10. Raytheon Technologies
11. Laboratory for Atmospheric and Space Physics, University of Colorado Boulder, Boulder, CO, USA
12. Department of Atmospheric and Oceanic Sciences, University of Colorado Boulder, Boulder, CO, USA
13. NASA Goddard Space Flight Center, Community Coordinated Modeling Center, Greenbelt, MD, USA
14. Physics Department, Catholic University of America, Washington, DC, USA
* Corresponding author, c.wright@bath.ac.uk

Abstract

The January 2022 Hunga Tonga–Hunga Ha'apai eruption was one of the most explosive volcanic events of the modern era[1,2], producing a vertical plume which peaked > 50km above the Earth. The initial explosion and subsequent plume triggered atmospheric waves which propagated around the world multiple times[add-ref-A]. A global-scale wave response of this magnitude from a single source has not previously been observed. Here we show the details of this response, using a comprehensive set of satellite and ground-based observations to quantify it from surface to ionosphere. A broad spectrum of waves was triggered by the initial explosion, including Lamb waves[3,4] propagating at phase speeds of 318.2 ± 6 ms^{-1} at surface level and between 308 ± 5 to 319 ± 4 ms^{-1} in the stratosphere, and gravity waves[5] propagating at 238 ± 3 to 269 ± 3 ms^{-1} in the stratosphere. Gravity waves at sub-ionospheric heights have not previously been observed propagating at this speed or over the whole Earth from a single source[6,7]. Latent heat release from the plume remained the most significant individual gravity wave source worldwide for >12 hours, producing circular wavefronts visible across the Pacific basin in satellite observations. A single source dominating such a large region is also unique in the observational record. The Hunga Tonga eruption represents a key natural experiment in how the atmosphere responds to a sudden point-source-driven state change, which will be of use for improving weather and climate models.

On the 15th of January 2022, the Hunga Tonga–Hunga Ha'apai submarine volcano (20.54°S, 175.38°W, hereafter 'Hunga Tonga') erupted, producing a vertical plume >30 km tall with overshooting tops above 55 km, a record in the satellite era[8] and likely longer[2]. From surface-pressure data, we estimate a single-event energy release from the initial explosion of between 10-28 EJ, likely larger than the 1991 Mt Pinatubo eruption[2] (~10 EJ), and possibly comparable to Krakatoa in 1883[2] (~30 EJ) (see Methods and Extended Data Figures 1a,b).

48 Large explosions such as volcanoes and nuclear tests are theoretically understood to produce
49 atmospheric waves[9,10] across a range of length and frequency scales. At horizontally-short
50 wavelengths, these include external Lamb waves[3,4,11] , acoustic waves[10] and internal gravity
51 waves[12]. In addition to explosion-generated waves, volcanoes can also act as a sustained
52 wave source after the initial eruption via updrafts and heating associated with plume
53 convection[13,14].

54 In practice, observations of such waves at sub-acoustic frequencies after volcanic eruptions
55 are rare. Krakatoa[4] and Pinatubo[15], amongst others, produced strong Lamb waves visible in
56 surface pressure. Internal waves in the boundary layer have been inferred from seismography,
57 barometry and infrasound for eruptions including El Chichon[13] (1982), Pinatubo[13] and
58 Okmok[14] (2008). In the free atmosphere, local gravity wave activity associated with plume
59 convection has been seen in mesospheric nightglow over the La Soufrière (2021) and
60 Calbuco[12] (2015) eruptions and in local cloud over eruptions including Cumbre Vieja (2021).
61 Re-examination of 1990s Advanced Very High Resolution Radiometer data also shows
62 waves in cloud above Pinatubo (Extended Data Figure 2). Finally, an electron-density
63 ionospheric wave response is usually observed[16,17], with the response magnitude proposed as
64 a metric of volcano explosive power[18,add-ref-D,add-ref-E,add-ref-F].

65 There is however no direct observational evidence for long-distance propagation in the free
66 electrically-neutral atmosphere of either Lamb or gravity waves triggered by volcanoes. Pre-
67 2000s satellite observations had insufficient resolution and coverage to measure such waves,
68 and no event since[6] has produced a wave response similar to that identified within hours[19] of
69 Hunga Tonga. This eruption thus represents an opportunity to quantify the wave response to a
70 point-source disruption at a scale and comprehensiveness unique in the observational record.

Eruption and Immediate Wave Response

72 Figures 1 and 2 show the propagation of Lamb and gravity waves triggered by the initial
73 eruption on the 15th of January, Figure 1 as height-integrated data from the Geostationary
74 Operational Environmental Satellite (GOES) and MeteoSat platforms and Figure 2 as height-
75 resolved measurements from multiple instrument types in addition to GOES.

76 The eruption became visible just after 04:00 UTC as a plume which reached a width of
77 200km and height of >30km within 30 minutes[8]. 20-30 minutes after the plume began rising,
78 an atmospheric wave became visible in ten-minute-resolution near-infrared geostationary
79 imagery. Back-projection from surface pressure data shows that the trigger source occurred at
80 04:28±0:02 UTC, with the leading wavefront propagating away at a near-surface phase speed
81 of 318.2 ± 6 ms^{-1} (Figure 2c, Extended Data Figure 1c,d, Supplementary Figure 1). Based on
82 the high phase speed, large amplitude and non-dispersive nature of the signal we identify this
83 as a Lamb wave. This type of wave is non-dispersive, and the observed speed is consistent
84 with the Lamb wave produced by Krakatoa, estimated[20] to have propagated at 318.8 ± 3 ms^{-1}.

85 The Hunga Tonga Lamb wave propagated around the globe, passing through the antipodal
86 point in Algeria 18.1 hours (±7.5 minutes) after the eruption (Figure 1). By this time, the
87 wavefront had deformed due to atmospheric and surface processes, and passed through the
88 antipode as four distinct wavefronts (Figure 1m-p). Over following days, it was tracked
89 propagating at least three times[21,add-ref-A] around the Earth. We also see a faint signal in GOES
90 data consistent with the wave being partially reflected from the Andes on its first transit
91 (Figure 1), and evidence of the wave being slowed over South America (Extended Data
92 Figure 10).

93   Using radiance data from the Advanced Infrared Sounder (AIRS), Cross-track Infrared
94   Sounder (CrIS) and Infrared Atmospheric Sounding Interferometer (IASI) polar-orbiting
95   thermal infrared (IR) sounders (specifically, 4.3μm data sensitive to altitudes ~39 km±5 km
96   and 15 μm data sensitive to the both ~25±5km and ~42±5km altitude levels separately,
97   Figure 2a), we see the Lamb wave as a high-amplitude monochromatic pulse with a phase
98   speed of between 308±5 and 319±4 ms^{-1} depending on location. We also observe it as a pulse
99   just above the noise floor of Cloud Imaging and Particle Size (CIPS) Rayleigh albedo
100   anomaly data 12 300km away from and 10.75 hours after the eruption (~55±5km altitude,
101   phase speed 316-319 ms^{-1}, Extended Data Figure 4a), and as phase fronts in hydroxyl airglow
102   over Hawai'i, 4960 km away from and 4.3 hours after (~87±4km altitude, phase speed 318
103   ms^{-1}).

104   The observed Lamb wave phase fronts are uniform in height and phase speed to within the
105   error range of each instrument from the surface to at least the upper mesosphere/lower
106   thermosphere. The energy density of a Lamb wave is theoretically expected[22] to decay
107   exponentially with height, and the observed phase speed is consistent with a vertical mean of
108   sound speed weighted according to this energy distribution (see Methods). Our data may
109   show evidence of a slightly different speed for propagation in different directions across the
110   Earth (e.g. at Broome, Australia, we measure 319 ms^{-1} for the westward-travelling wave and
111   316 ms^{-1} for the eastward, Extended Data Figure 1e), but this is within the uncertainty range
112   of our measurements. The asymmetric perturbations we observe are consistent in sign with
113   such a shift due to background winds.

114   Following the Lamb wave, we observe a series of slower waves with continually varying
115   speeds and horizontal wavelengths (λ_h) that we identify as a dispersive packet of fast internal
116   gravity waves (Figure 2a). These have phase speeds of 240-270 ms^{-1}, varying with local λ_h.
117   The leading phase front has the largest amplitude and longest λ_h, with a brightness
118   temperature (BT) amplitude of 0.74 K and λ_h of 380 km here falling to 0.15 K and 100 km
119   across the packet width. This packet is observed to extend ~2000 km and eight phase cycles
120   across the South Pacific ~7 hours after generation (Extended Data Figure 5). We observe the
121   packet over multiple orbits of AIRS, CrIS, and IASI across the globe, in CIPS over
122   Antarctica, and in airglow (~85km altitude, depth ~8km) above Hawai'i. Vertical wavelength
123   (λ_z) is poorly defined but very deep: no phase difference is seen between AIRS observations
124   at 25 and 42 km altitude, and calculations based on observed speed and λ_h imply $\lambda_z \gg 110$
125   km, i.e. greater than the depth of the homosphere. These phase speeds are consistent with
126   vertically-propagating gravity waves travelling at speeds close to, but very slightly less than,
127   the theoretical maximum speeds achievable prior to total internal reflection (See Methods and
128   Extended Data Figure 6) and with the same temporal origin and source as the Lamb wave.

129   This leading gravity wave packet passes through the antipode at times between ~00:30 and
130   02:30 UTC on the 16th of January, i.e. 20-22 hours after the eruption (Extended Data Figures
131   7a-c), with the broad time window determined by separation of different λ_h components with
132   time. Gravity waves remaining coherent and expanding over the whole globe from a single
133   source of any kind are unprecedented in the observational record[6]. On their return journey
134   from the antipode, the waves become difficult to distinguish in our intermittent low-Earth
135   orbit satellite snapshots from those produced both later by Hunga Tonga and by other
136   sources, and consequently we cannot track them to their extinction.

137   The gap between the initial Lamb wave and subsequent gravity wave grows with time. This is
138   consistent with a theoretically-predicted forbidden phase speed range between external Lamb
139   wave and internal gravity wave limits imposed by total internal reflection (Extended Data
140   Figure 6). Two low-amplitude wavefronts are present in the gap; these propagate with the

141   same speed as the leading Lamb wavefront, but trace back to different origin times (Figure 2a
142   and Extended Data Figure 4b). We therefore identify these as Lamb waves triggered by
143   subsequent smaller explosions which were also observed in local surface pressure (Extended
144   Data Figure 8).

145   Ionospheric data (Figure 2d and Extended Data Figure 3) show key differences from the
146   lower atmosphere. Over New Zealand, we see three large travelling ionospheric disturbances
147   (TIDs), with phase speeds, λ_h and amplitudes of (1) 667 ms^{-1}, 1000 km, 0.2 TEC Units
148   (TECu); (2) 414 ms^{-1}, 700 km, 0.4 TECu and (3) 343 ms^{-1}, 400 km and >1 TECu
149   respectively. The speed and propagation direction of these waves is consistent with a Hunga
150   Tongan source between 04:15 and 05:00, but do not share the arrival time, phase speed or λ_h
151   of the Lamb wave in other atmospheric layers. Therefore, we do not identify these TIDs as
152   the Lamb wave. However, a strong and brief TEC modulation, spiking at an amplitude of
153   >0.6 TECu, is seen at 06:15 consistent with the expected arrival time and brief period of the
154   Lamb wave.

155   We do not see TID 1 over North America, but do see a signal consistent with TID 2 and
156   another TID (4) with phase speed ~311 m/s which is also consistent with TIDs measured over
157   New Zealand. We again see a strong TEC modulation at the expected Lamb wave arrival
158   time.

159   The properties of TIDs 1 and 2 are inconsistent with slant path gravity waves propagating
160   from Hunga Tonga, but these TIDs could have reached the observed sites by indirect paths,
161   e.g. by vertically propagating as acoustic or gravity waves above the volcano then travelling
162   at high horizontal speeds through the ionosphere. The properties of TIDs 3 and 4 are
163   consistent with the wave activity generated over Hunga Tonga in the hours after the primary
164   eruption.

Sustained Post-Eruption Wave Generation

166   After the initial trigger, sustained gravity wave generation is seen in the clouds above Hunga
167   Tonga and radiating outwards across the Pacific basin. While smaller in amplitude and slower
168   in phase speed than those from the initial eruption, these waves are also highly anomalous
169   relative to past gravity wave observations.

170   Figure 3 shows BT measurements from (a-d) the GOES 10.3μm channel over the Hunga
171   Tonga area and (e-g) the AIRS, CrIS and IASI 4.3μm stratospheric channels over the Pacific
172   basin for selected times.

173   In GOES observations of the eruption cloud top (Figure 3a-c, Supplementary Figure 3), arced
174   features consistent in morphology and temporal progression with propagating concentric
175   gravity wave phase fronts are visible. λ_h ranges from the 8km resolution limit of the data to
176   65km, and BT amplitude from 0.5-8K. These measured properties are very similar to those of
177   gravity waves generated near the convective centres of hurricanes.

178   The apparent centre of these waves is slightly west of Hunga Tonga. This is consistent with
179   refraction of the wave field by the prevailing easterly winds. The waves are remarkably
180   consistent in concentric shape over several hours, suggesting a powerful and relatively
181   persistent pulsing source for wave generation. The source may be pulses of convection
182   within the plume above the volcano. The waves weaken in amplitude over time, particularly
183   after 15:00UTC, but are visible until at least 19:20 UTC (Figure 3d). They are not found on
184   subsequent days. These results suggest that the volcano may have created a sustained source
185   of convectively-generated waves for nearly fifteen hours after the initial eruption.

186 Stratospheric AIRS, CrIS and IASI observations (Figure 3e-g, Extended Data Figure 7d-o)
187 show wave activity across a range of spatial, frequency and amplitude scales throughout the
188 Pacific basin, all centred on Hunga Tonga. Tracking individual phase fronts is challenging as
189 these data are near-instantaneous at any given location, but conservatively the distribution
190 must include a large fraction of waves with phase speeds >100 ms^{-1}. For example, small-scale
191 continuous wavefronts centred on Hunga Tonga are clearly visible near Japan before 16:00 in
192 Figure 3g and, even if emitted at the earliest possible time of 04.28 UTC, must have phase
193 speeds ~200 ms^{-1} to have travelled this far. Unlike more typical observed waves, these waves
194 can therefore propagate with little apparent influence from global wind patterns due to their
195 unusually large phase speeds. Such fast speeds reduce normal dissipation effects, allowing
196 the waves to propagate vast distances and affect much higher altitudes than typical gravity
197 waves.

198 These waves dominate the stratospheric gravity wave spectrum over a radius >9000km for
199 >12 hours (Extended Data Figure 7d-o). This is exceptional for a single source, and unique in
200 our observational record[6,7]. Orographic wave sources often persist for longer, but are spatially
201 localised; while some waves in the southern polar jet may have propagated downstream[23,24]
202 or laterally [6,25] from orographic sources, the area they affect is an order of magnitude smaller
203 than here and the waves themselves highly intermittent. Waves from non-orographic sources
204 such as tropical convection and extreme events such as hurricanes, meanwhile, typically
205 become indistinguishable from background within 2000-3500 km[26–27].

How were the waves generated?

207 Although we cannot directly observe the generation of the waves due to insufficient temporal
208 resolution (for the initial explosion) and ash plume blocking effects (for both the initial
209 explosion and subsequent wave generation), the observed wave properties and context allow
210 us to infer likely mechanisms by which they were generated.

211 The strong initial response is likely due to the eruption's shallow submarine context and large
212 explosive power. As the volcanic vent was only tens to hundreds of metres below water[28] the
213 seawater did not suppress the blast but was instead flash-boiled[29] and propelled into the
214 stratosphere. Here it condensed, releasing latent heat near-instantaneously across a depth of
215 tens of kilometres. This strong and short-lived forcing would produce vertically-deep waves
216 across a broad spectrum, consistent with observations. This mechanism is also consistent with
217 significant and large IASI-observed increases in stratospheric water vapour (Extended Data
218 Figure 9), and H_2SO_4 in the plume relative to what would be expected for an eruption of this
219 size, which is in turn consistent with sulfuric acid forming in situ due to insufficient
220 volcanogenic SO_2 release and the time available to produce H_2SO_4.

221 Subsequent wave generation is likely due to similar processes as standard convective waves,
222 such as mechanical oscillator effects[30] associated with vertical air motion within the plume or
223 pulsing from the volcanic heat source below. Such forces would produce sufficiently strong
224 perturbations to generate gravity waves visible both in the plume and propagating freely
225 away. Such a mechanism is again consistent with our observations, particularly the similarity
226 in morphology and amplitude of the observed waves to the concentric generated by
227 hurricanes[add-ref-G,add-ref-H] and convective weather systems[27,add-ref-I].

228 Another possibility is that the eruptive energy could have transferred to tsunami waves and
229 the tsunamis in turn have generated the waves we observe[add-ref-K]. However, we argue that this
230 is less likely than simple linear propagation from a convective atmospheric source due to the
231 highly regular concentric nature of the observed atmosphere waves in Figures 3e-g, which
232 show no significant evidence of tsunami deformation effects. Other studies have shown that

233 the atmospheric waves also generated meteotsunamis in both the Pacific and other basins[add-
234 ref-L,add-ref-M], highlighting the complex interplays between ocean and atmospheric waves in the
235 Earth system.

Weather and Climate Forecasting Implications

237 While in recent years we have been able to routinely characterise gravity waves in
238 observational data, understanding how the observed spectrum at a location arises has been
239 complicated by fundamental problems in distinguishing the source of a wave from the
240 pathway it has taken to the observation[24]. Being able to separate these problems would lead to
241 major advances in simulating and parameterising gravity waves in next-generation weather
242 and climate models. The Hunga Tonga eruption represents an important natural experiment in
243 this area. The volcano was a clearly-identifiable near-point source, produced gravity waves
244 across a broad range of spatiotemporal and frequency scales, and these waves were observed
245 by a diverse constellation of instruments worldwide.

246 While the $\gtrsim 150 \text{ms}^{-1}$ phase speed waves produced by the initial eruption are unusual for
247 heights below the mesosphere, models in current use do routinely parameterise gravity waves
248 with phase speeds as high as 100 ms^{-1} at altitudes as low as 16 km[add-ref-O], similar to a large
249 fraction of those we observe after the main eruption. In addition, waves in the poorly-
250 instrumented mesosphere and above can routinely have speeds of hundreds of metres per
251 second[add-ref-Q], and observations of this extreme case in the better-instrumented stratosphere
252 could provide useful insight for research in this area.

253 As such, simulating this eruption in atmospheric models, whether as a point convective
254 source or in a dedicated volcanic simulation, could provide major insight into the strengths
255 and deficiencies of models. While current-generation global-scale weather models cannot
256 reproduce these waves due to their relatively-limited spatial and temporal resolution and the
257 Courant-Friedrichs-Lewy condition, the waves can be directly resolved by specialist large
258 eddy simulations[add-ref-P] and similar specialist models[add-ref-Q], albeit only currently for
259 relatively small geographic regions.

260 Finally, we note that the propagation of these waves can also be used as a test of how well
261 models reproduce the bulk atmosphere, by comparing modelled and observed propagation
262 delays for both the Lamb and gravity waves. These could provide important information
263 quantifying how well current and future models represent atmospheric winds, temperatures
264 and density structures, particularly if constrained to the initial conditions of the 15th of
265 January 2022.

266

267

268

Main References

270 1. Poli, P. & Shapiro, N. M. Rapid characterization of large volcanic eruptions: measuring
271   the impulse of the Hunga Tonga explosion from teleseismic waves.
272   http://www.essoar.org/doi/10.1002/essoar.10510358.1 (2022)
273   doi:10.1002/essoar.10510358.1.
274 2. Pyle, D. M. Sizes of Volcanic Eruptions. in The Encyclopedia of Volcanoes 263–269
275   (Elsevier, 2000).
276 3. Garrett, C. J. R. Atmospheric edge waves. Q.J Royal Met. Soc. **95**, 731–753 (1969).

4. The Eruption of Krakatoa and Subsequent Phenomena. Q.J.R. Meteorol. Soc. **14**, 301–307 (1888).

5. Fritts, D. C. & Alexander, M. J. Gravity wave dynamics and effects in the middle atmosphere. Rev. Geophys. **41**, 1003 (2003).

6. Hindley, N. P., Wright, C. J., Hoffmann, L., Moffat-Griffin, T. & Mitchell, N. J. An 18-Year Climatology of Directional Stratospheric Gravity Wave Momentum Flux From 3-D Satellite Observations. Geophys. Res. Lett. **47**, (2020).

7. Ern, M. et al. GRACILE: a comprehensive climatology of atmospheric gravity wave parameters based on satellite limb soundings. Earth Syst. Sci. Data **10**, 857–892 (2018).

8. Carr, J. L., Horvath, A., Wu, D. L. & Friberg, M. D. Stereo Plume Height and Motion Retrievals for the Record-Setting Hunga Tonga-Hunga Ha'apai Eruption of 15 January 2022. Geophys. Res. Lett. **49**, e2022GL098131 (2022)

9. Press, F. & Harkrider, D. Air-Sea Waves from the Explosion of Krakatoa. Science **154**, 1325–1327 (1966).

10. Pfeffer, R. L. & Zarichny, J. Acoustic-Gravity Wave Propagation from Nuclear Explosions in the Earth's Atmosphere. J. Atmos. Sci. **19**, 256–263 (1962).

11. Kanamori, H. & Given, J. W. Lamb pulse observed in nature. Geophys. Res. Lett. **10**, 373–376 (1983).

12. Miller, S. D. et al. Upper atmospheric gravity wave details revealed in nightglow satellite imagery. Proc Natl Acad Sci USA **112**, E6728–E6735 (2015).

13. Widmer, R. & Zürn, W. Bichromatic excitation of long-period Rayleigh and air waves by the Mount Pinatubo and El Chichon volcanic eruptions. Geophys. Res. Lett. **19**, 765–768 (1992).

14. De Angelis, S., McNutt, S. R. & Webley, P. W. Evidence of atmospheric gravity waves during the 2008 eruption of Okmok volcano from seismic and remote sensing observations: Gravity Waves at Okmok Volcano. Geophys. Res. Lett. **38** (2011).

15. Watada, S. & Kanamori, H. Acoustic resonant oscillations between the atmosphere and the solid earth during the 1991 Mt. Pinatubo eruption. J. Geophys. Res. **115**, B12319 (2010).

16. Astafyeva, E. Ionospheric Detection of Natural Hazards. Rev. Geophys. 2019RG000668 (2019) doi:10/gghhwc.

17. Themens, D. R. et al. Global propagation of ionospheric disturbances associated with the 2022 Tonga Volcanic Eruption. Geophys. Res. Lett. **49** e2022GL098158 (2022), doi: 10.1029/2022GL098158

18. Manta, F. et al. Correlation Between GNSS-TEC and Eruption Magnitude Supports the Use of Ionospheric Sensing to Complement Volcanic Hazard Assessment. J Geophys Res Solid Earth **126**, (2021).

19. Adam, D. Tonga volcano eruption created puzzling ripples in Earth's atmosphere. Nature d41586-022-00127–1 (2022) doi:10/gn8ktd.

20. Taylor, G. I. Waves and tides in the atmosphere. Proc. R. Soc. Lond. A **126**, 169–183 (1929).

21. Lin, J.-T. et al. Rapid Conjugate Appearance of the Giant Ionospheric Lamb Wave in the Northern Hemisphere After Hunga-Tonga Volcano Eruptions. http://www.essoar.org/doi/10.1002/essoar.10510440.1 (2022) doi:10.1002/essoar.10510440.1.

22. Bretherton, F. P. Lamb waves in a nearly isothermal atmosphere. Q.J Royal Met. Soc. 95, 754–757 (1969).

324   23. Hindley, N. P., Wright, C. J., Smith, N. D. & Mitchell, N. J. The southern stratospheric
325   gravity wave hot spot: individual waves and their momentum fluxes measured by
326   COSMIC GPS-RO. Atmos. Chem. Phys. **15**, 7797–7818 (2015).
327   24. Wright, C. J., Hindley, N. P., Hoffmann, L., Alexander, M. J. & Mitchell, N. J. Exploring
328   gravity wave characteristics in 3-D using a novel S-transform technique: AIRS/Aqua
329   measurements over the Southern Andes and Drake Passage. Atmos. Chem. Phys. **17**,
330   8553–8575 (2017).
331   25. Plougonven, R., la Cámara, A., Hertzog, A. & Lott, F. How does knowledge of
332   atmospheric gravity waves guide their parameterizations? Q.J.R. Meteorol. Soc **146**,
333   1529–1543 (2020).
334   26. Wright, C. J. Quantifying the global impact of tropical cyclone-associated gravity waves
335   using HIRDLS, MLS, SABER and IBTrACS data. Q.J.R. Meteorol. Soc. **145**, 3023–3039
336   (2019).
337   27. Stephan, C. & Alexander, M. J. Realistic simulations of atmospheric gravity waves over
338   the continental U.S. using precipitation radar data. J. Adv. Model. Earth Syst. **7**, 823–835
339   (2015).
340   28. Colombier, M. et al. Vesiculation and Quenching During Surtseyan Eruptions at Hunga
341   Tonga-Hunga Ha'apai Volcano, Tonga. J. Geophys. Res. Solid Earth **123**, 3762–3779
342   (2018).
343   29. Witze, A. Why the Tongan eruption will go down in the history of volcanology. Nature
344   d41586-022-00394-y (2022) doi:10/gpfhcm.
345   30. Fovell, R., Durran, D. & Holton, J. R. Numerical Simulations of Convectively Generated
346   Stratospheric Gravity Waves. J. Atmos. Sci. **49**, 1427–1442 (1992).
347
348

349   **Hey, I just read them and this is crazy, but here's some references to add in maybe:**

350   add-ref-A[1] – used!

351   add-ref-C[3] – used in methods.

352   add-ref-D[4] – used!

353   add-ref-E[5] – used!

354   add-ref-F[6] – used!

355   add-ref-G[7] – used!

356   add-ref-H[8] – used!

357   add-ref-I[9] – used!

358   add-ref-J[10] – used!

359   add-ref-K[11] – used!

360   add-ref-L[12] – used!

361   add-ref-M[13] – used!

362   add-ref-O[15] – used!

363   add-ref-P[16] – used!

364   add-ref-Q[17] – used!

365   1. Harrison, G. Pressure anomalies from the January 2022 Hunga Tonga-Hunga Ha'apai eruption.

366   *Weather* **77**, 87–90 (2022).

367   2. Otsuka, S. Visualizing Lamb waves from a volcanic eruption using meteorological satellite

368   Himawari-8. *Geophysical Research Letters* (2022) doi:10.1029/2022GL098324.

369   3. Swenson, G. R., Alexander, M. J. & Haque, R. Dispersion imposed limits on atmospheric gravity

370   waves in the mesosphere: Observations from OH airglow. *Geophys. Res. Lett.* **27**, 875–878 (2000).

371   4. Roberts, D. H., Klobuchar, J. A., Fougere, P. F. & Hendrickson, D. H. A large-amplitude traveling

372   ionospheric disturbance produced by the May 18, 1980, explosion of Mount St. Helens. *J.*

373   *Geophys. Res.* **87**, 6291 (1982).

374   5. Liu, C. H. *et al.* Global dynamic responses of the atmosphere to the eruption of Mount St. Helens

375   on May 18, 1980. *J. Geophys. Res.* **87**, 6281 (1982).

376   6. Igarashi, K. *et al.* Ionospheric and atmospheric disturbances around Japan caused by the eruption

377   of Mount Pinatubo on 15 June 1991. *Journal of Atmospheric and Terrestrial Physics* **56**, 1227–

378   1234 (1994).

379   7. Hoffmann, L., Wu, X. & Alexander, M. J. Satellite Observations of Stratospheric Gravity Waves

380   Associated With the Intensification of Tropical Cyclones. *Geophys. Res. Lett.* **45**, 1692–1700

381   (2018).

382   8. Tratt, D. M. *et al.* GHOST: A Satellite Mission Concept for Persistent Monitoring of Stratospheric

383   Gravity Waves Induced by Severe Storms. *Bulletin of the American Meteorological Society* **99**,

384   1813–1828 (2018).

385   9. Stephan, C. C. *et al.* Intercomparison of Gravity Waves in Global Convection-Permitting Models. *J.*

386   *Atmos. Sci.* **76**, 2739–2759 (2019).

387   10.   Rolland, L. M. *et al.* The resonant response of the ionosphere imaged after the 2011 off the

388   Pacific coast of Tohoku Earthquake. *Earth Planet Sp* **63**, 853–857 (2011).

389   11.   Inchin, P. A., Heale, C. J., Snively, J. B. & Zettergren, M. D. The Dynamics of Nonlinear

390   Atmospheric Acoustic-Gravity Waves Generated by Tsunamis Over Realistic Bathymetry. *J.*

391   *Geophys. Res. Space Physics* **125**, (2020).

392   12.   Ramírez-Herrera, M. T., Coca, O. & Vargas-Espinosa, V. Tsunami Effects on the Coast of

393   Mexico by the Hunga Tonga-Hunga Ha'apai Volcano Eruption, Tonga. *Pure Appl. Geophys.* (2022)

394   doi:10.1007/s00024-022-03017-9.

395   13.   Yuen, D. A. *et al.* Under the surface: Pressure-induced planetary-scale waves, volcanic

396   lightning, and gaseous clouds caused by the submarine eruption of Hunga Tonga-Hunga Ha'apai

397   volcano. *Earthquake Research Advances* 100134 (2022) doi:10.1016/j.eqrea.2022.100134.

398   14.   Jackson, D. R. *et al.* Future Directions for Whole Atmosphere Modeling: Developments in the

399   Context of Space Weather. *Space Weather* **17**, 1342–1350 (2019).

400   15.   Richter, J. H., Sassi, F. & Garcia, R. R. Toward a Physically Based Gravity Wave Source

401   Parameterization in a General Circulation Model. *Journal of the Atmospheric Sciences* **67**, 136–156

402   (2010).

403   16.   O'Neill, M. E., Orf, L., Heymsfield, G. M. & Halbert, K. Hydraulic jump dynamics above

404   supercell thunderstorms. *Science* **373**, 1248–1251 (2021).

405   17.   Fritts, D. C., Lund, T. S., Lund, A. C. & Yudin, V. Impacts of Limited Model Resolution on the

406   Representation of Mountain Wave and Secondary Gravity Wave Dynamics in Local and Global

407   Models. Part 1: Mountain Waves in the Stratosphere and Mesosphere. *JGR Atmospheres* (2022)

408   doi:10.1029/2021JD035990.
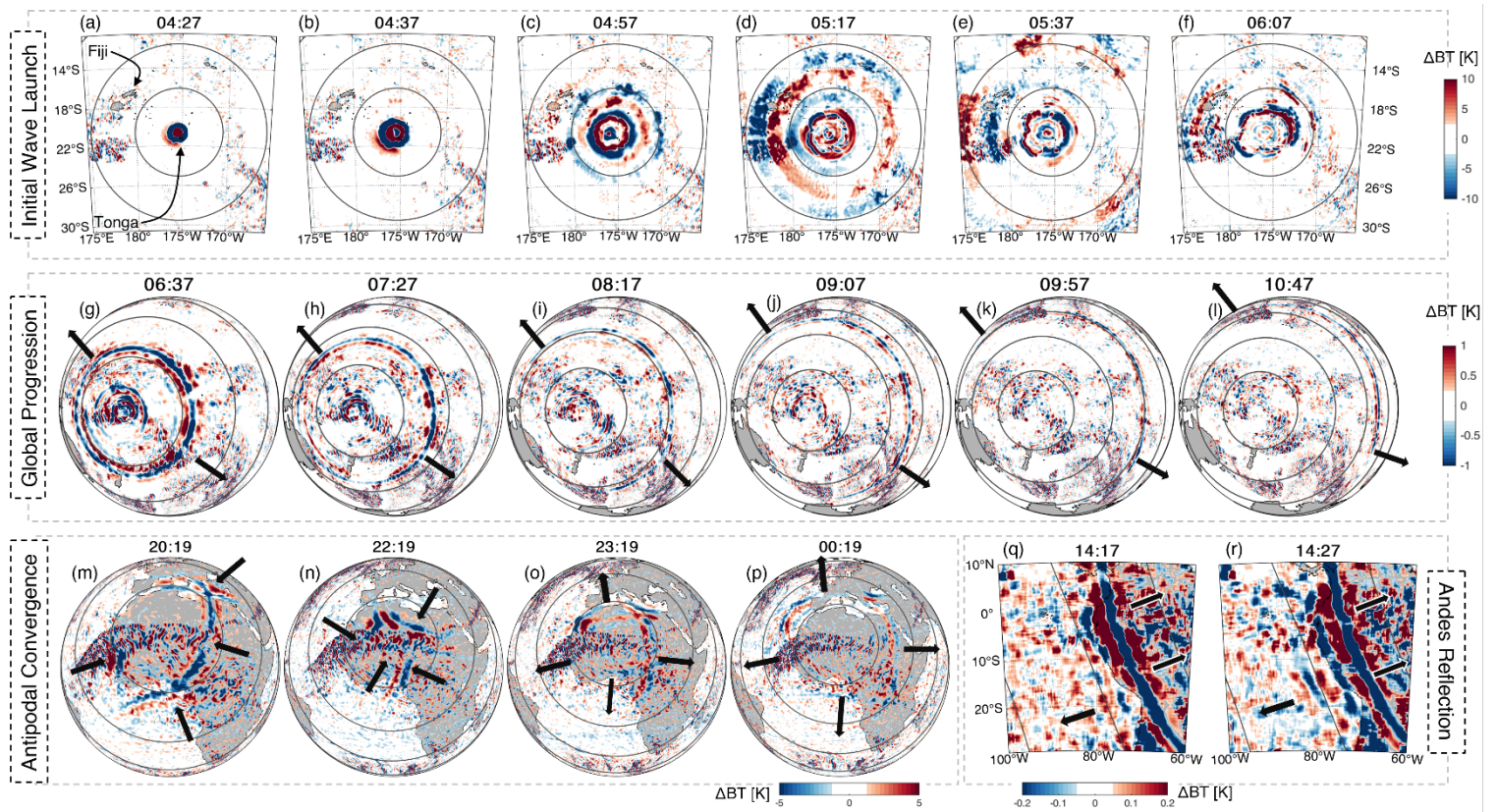
Figure 1: **Initial Lamb wave propagation in the troposphere**: *Brightness temperature changes observed by (top two rows) GOES, (bottom left) Meteosat Spinning Enhanced Visible and InfraRed Imager (SEVIRI) and (bottom right) GOES-EAST. Range rings indicate distance from Hunga Tonga in (top row) 500km and (lower rows) 2000km steps. To reduce noise from weather systems, global and antipodal panels have been processed with a 200km-radius Wiener filter, and Andes panels with a 400km boxcar and 72-km-radius Wiener filter. Black arrows indicate approximate wave location and propagation direction. All times UTC.*

409
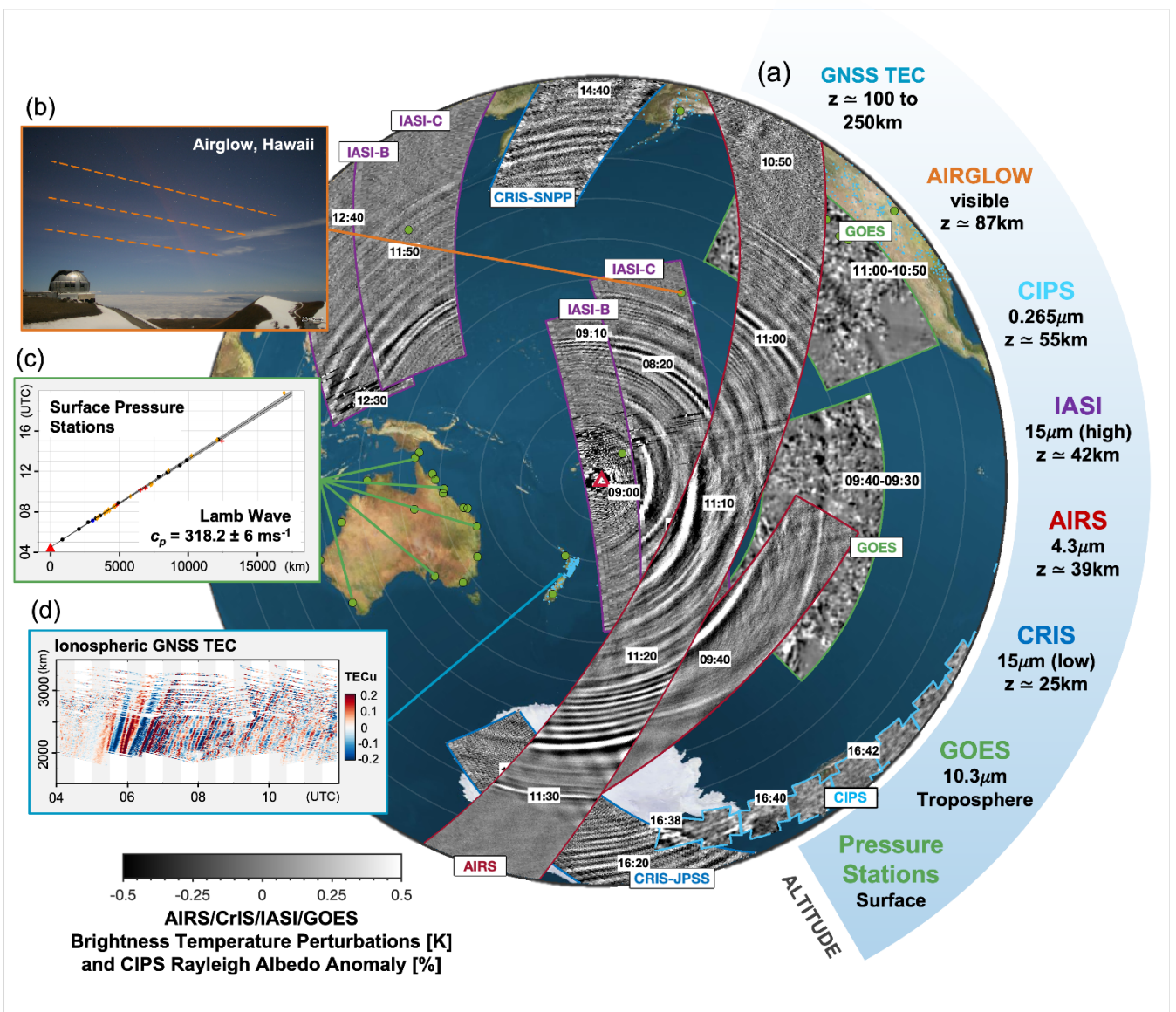
*Figure 2: **Initial gravity and Lamb wave propagation at all heights:** Combined measurements of the initial wave release as osberved by multiple platforms, listed with their approximate altitudes at right and at times as indicated by overlaid text labels. Inset panels showing pressure (green outline) and TEC (blue outline) distance/time series are reproduced as Extended Data Figures 1d and 3 respectively. Note that AIRS, CrIS and IASI all measure the same three stratospheric altitude channels, but only one is used here from each instrument to show all levels while maintaining visual clarity; due to the long vertical wavelengths of the observed waves, all three levels are near-identical. Airglow inset shows a northward view containing the Lamb wavefront at 09:20 UTC, ~30 minutes after the wave passed overhead.*
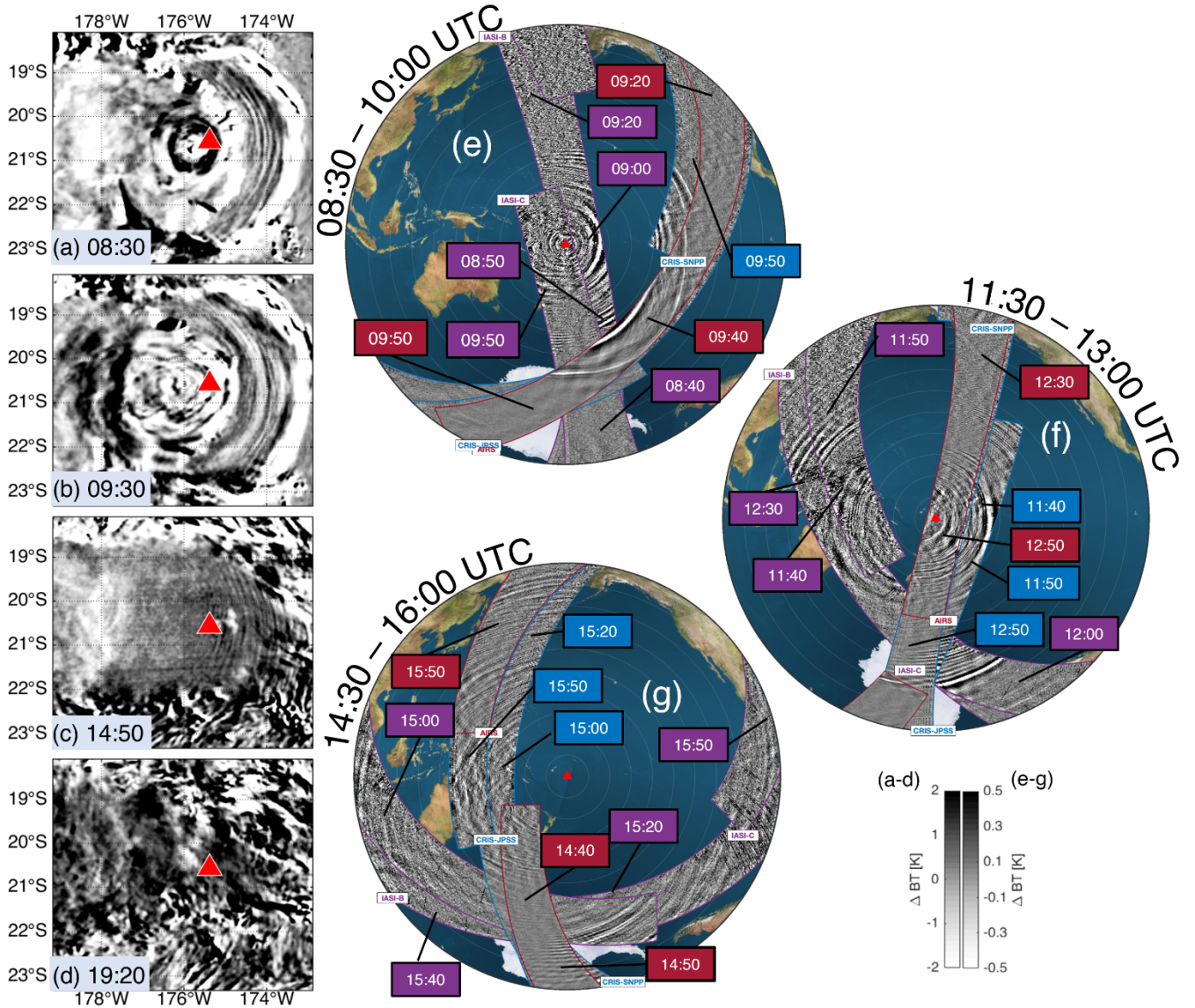
Figure 3: **Post-eruption wave activity**: *(a-d) in and around the volcanic plume as observed by GOES and (e-g) over the entire Pacific basin as observed by AIRS, CrIS and IASI. For (e-g,) coloured labels indicate individual satellite overpass times for context, with AIRS labelled in red, CrIS in blue and IASI in purple. Note that the colour scales in panels (a) and (b) saturate significantly, and values extend to ±8K.*

411

Methods

Explosive Energy Estimate from Surface Pressure Data

We estimate the explosive energy associated with the eruption using three separate approaches. All three give a value in the range 10-28 EJ.

1. Waveform based on a nuclear explosion: Posey and Pierce (1971)[33] suggested that the energy yield of an explosion in the atmosphere can be calculated as $E = 13p\sqrt{[r_e \sin(r/r_e)]}H_s(CT)^{3/2}$, where p is the measured pressure anomaly, r the distance from the explosion, r_e the Earth's radius, H_s the atmospheric scale height, c the speed of the wave, and T the time separation between the first and second peaks of the pressure disturbance. From available pressure-station data at distances ranging from 2500-17500 km from Hunga Tonga (Extended Data Figure 1b), this provides an estimate of ~20±8 EJ.

2. Waveform based on previous volcanic eruptions: Gorshkov (1960)[34] estimated the explosive energy of a volcanic eruption as $E = \frac{2\pi H_s \sin(\theta)}{\rho c}\int_{t1}^{t2} p^2\, dt$, where θ is the distance from the eruption in degrees, ρ the Earth's surface air density, t is time, and t1 and t2 are the start and end times of the anomaly (different for each station). This gives an estimate of ~10EJ.

3. Estimated pressure force: assuming the pressure anomaly spreads under an even cloud of area A, then the work done by the pressure impulse over a column of height h_c is $W = pAh_c$. For an area of radius 200 km and pressure change of 5 hPa, this gives a work estimate ~18 EJ.

Estimate of Lamb Wave Phase Speed

We use the approach of Bretherton (1969)[22] and initial-release data from the European Centre for Medium-Range Weather Forecasts' Fifth-Generation Reanalysis (ERA5T) to calculate the expected speed of the Lamb wave. We first compute the local speed of sound as $c_s(z) = k\sqrt{T}$, where z is the altitude, T the local temperature and k=20.05 ms^{-1}K$^{-1/2}$. For a Lamb wave, where energy density decays exponentially with height, energy density is $E(z) = C\,exp(-z/H)$, where C is a constant term which subsequently cancels in our calculation, and H is

$$H = \frac{c_s^2}{(2-\gamma)}g,$$

for a ratio of specific heats γ which we set to 1.4, and acceleration due to gravity g which we set to 9.80665ms^{-1}. We then calculate the phase speed of the Lamb wave as a vertical mean of the speed of sound weighted by energy density, i.e.

$$c_m^2 = \frac{\int_0^\infty [c_s(z)+u(z)]^2 E(z)\, dz}{\int_0^\infty E(z)\, dz},$$

where u is the local wind speed.

For ERA5T meteorological output for the 15th of January 2022 at the 04:00 UTC timestep, this gives a phase speed of 313-318 ms^{-1}. Similar results are obtained using the 05:00 UTC timestep. Our calculation omits the contribution of altitudes above 80 km to the energy density calculation as ERA5 data do not extend above this level, but as energy density decreases exponentially with height this contribution should be small.

Gravity Wave Speed Limit Calculation

Linear wave solutions to the Navier-Stokes equations of the form $A \exp[i(kx + mz - \hat{\omega}t)]$ satisfy the dispersion relation [22] of Fritts and Alexander (2003)[5], which is fourth-order in intrinsic frequency $\hat{\omega}$. For higher-frequency waves where $f^2 \ll \hat{\omega}^2$ and simplifying to planar 2D propagation, i.e. $l = 0$, we can rewrite this as a fourth-order equation in intrinsic phase speed $\hat{c} = \hat{\omega}/k$, i.e.

$$\frac{\hat{c}^4}{c_s^2} - \hat{c}^2 \left(1 + \frac{1}{4H^2k^2} + \frac{m^2}{k^2}\right) + \frac{N^2}{k^2} = 0.$$

Letting $x = \hat{c}^2$ gives a quadratic form of the equation

$$ax^2 + bx + c = 0$$

where $a = 1/c_s^2$, $b = -(1 + 1/(4H^2k^2) + m^2/k^2)$ and $c = N^2/k^2$, with solution

$$\hat{c}^2 = \frac{-b \pm \sqrt{b^2 - 4ac}}{2a}.$$

The positive root describes acoustic wave solutions and the negative root internal gravity waves. Allowing vertical wavenumber $m \to 0$ gives the curve $\hat{c}_{max}(k)$, the maximum phase speed for gravity waves before total internal reflection would prevent their vertical propagation. This limit is

$$\hat{c}_{max}^2 = \frac{c_s^2}{2}\left[1 + (4H^2k^2)^{-1} - \sqrt{[1 + 1/(4H^2k^2)]^2 - 4N^2/(c_s^2k^2)}\right]$$

and is shown as a function of horizontal wavelength k^{-1} in Extended Data Figure 6. Our results for the wave properties produced by Hunga Tonga are consistent with previous theoretical work considering normalised full spectra of acoustic and gravity waves[35,add-ref-C].

Airglow Imagery Processing

Airglow data have been obtained from the all-night cloud cameras at the Gemini Observatory on Mauna Kea, Hawaii. This assumed height layer is based on the colour of the airglow and spectral range of the cameras used at Gemini, which are both consistent with the hydroxyl (OH) airglow layer. There are five such cameras, one of which is aimed at a near-vertical angle (with a slight offset determined from study of the star field), and we use this image to identify the arrival time of the first wave packet using the image time stamp - this time is 08:48:53 UTC. At a distance of 4964 km and using an explosion time of 04:28:48 UTC, this gives a phase speed of 318.12 m/s. Further analysis using the other four cameras from the Gemini observatory gives results consistent with this.

AIRS, CRIS and IASI

We use brightness temperature observations associated with radiances in the 4.3 μm and 15 μm carbon dioxide absorption bands of AIRS, CrIS, IASI-B and IASI-C[31] on the 15th of January. These instruments can directly resolve stratospheric waves with vertical wavelengths $\gtrsim$15km and horizontal wavelengths $\gtrsim$30km, and typically provide twice-daily near-global coverage for each instrument in near-real time with an orbit approximately every 90 minutes. Perturbation fields suitable for spectrally and visually analysing wave signatures are produced by subtracting a fourth-order polynomial in the across-track direction from the data, consistent with previous work using these data[6,32].

CIPS

Imagery from the nadir-viewing CIPS instrument is analysed for the presence of deviations from a smooth model background of Rayleigh scattered UV sunlight (265 nm). The model removes the geometrical dependence of the observation and large-scale geophysical variability of the observed albedo. The data are binned to a uniform 7.5x7.5 km grid, allowing for observations down to 15 km horizontal wavelength. The altitude kernel limits sensitivity to vertical wavelengths $\gtrsim$10km, with a mean altitude of the contribution at ~55 km altitude. The satellite is in a sun synchronous polar orbit with an equator crossing currently near noon.

GOES/MeteoSat

We use data from band 13 of GOES-EAST and GOES-WEST, and band 5 of Meteosat-SEVIRI. These instruments image the Earth's disc at a spatial resolution of 2 km and a temporal resolution of 10 minutes (15 minutes for SEVIRI). Raw radiance data have been converted to brightness temperatures based on the centre wavelength of the channel filters, and then differenced between adjacent timesteps to highlight wave structure.

TEC

Total electron content observations were derived from dual-frequency GPS receivers in the New Zealand GeoNet and the NOAA CORS Networks. Satellite to ground GPS signals were processed following the method of Afraimovich et al. (2000)[36], and the dTEC values are projected onto an ionospheric shell altitude of 250 km, chosen to be near the F-layer peak height[add-ref-J]. The dTEC are then analysed to investigate the travelling ionospheric disturbance parameters.

Data Availability

Airglow data are available from https://www.gemini.edu/sciops/telescopes-and-sites/weather/mauna-kea/cloud-cam/allnightlong.html. They were obtained under a Creative Commons Attribution 4.0 International License issued by the NSF's NoirLab.

AIRS and CrIS data are available from the NASA Goddard Earth Sciences Data and Information Services Center: https://disc.gsfc.nasa.gov/.

CIPS data are available from the Laboratory for Atmospheric and Space Physics at the University of Colorado Boulder: https://lasp.colorado.edu/aim/.

ERA5 data are available from the Climate Data Store, https://cds.climate.copernicus.eu.

GOES data are available from the NOAA Geostationary Satellite Server, https://www.goes.noaa.gov/.

IASI data are available from the IASI Portal, https://iasi.aeris-data.fr/.

Surface Pressure data are included as a Supplementary file to this manuscript.

TEC data are available from https://www.geonet.org.nz/ and https://geodesy.noaa.gov/CORS/.

Methods References

31. Hoffmann, L. et al. Intercomparison of stratospheric gravity wave observations with AIRS and IASI. Atmos. Meas. Tech. **7**, 4517–4537 (2014).

530   32. Alexander, M. J. & Barnet, C. Using Satellite Observations to Constrain
531   Parameterizations of Gravity Wave Effects for Global Models. Journal of the Atmospheric
532   Sciences **64**, 1652–1665 (2007).
533   33. Posey, J. W. & Pierce, A. D. Estimation of Nuclear Explosion Energies from
534   Microbarograph Records. Nature **232**, 253–253 (1971).
535   34. Gorshkov, G. S. Determination of the explosion energy in some volcanoes according to
536   barograms. Bull Volcanol **23**, 141–144 (1960).
537   35. Yeh, K. C. & Liu, C. H. Acoustic-gravity waves in the upper atmosphere. Rev. Geophys.
538   **12**, 193 (1974).
539   36. Afraimovich, E.L. et al. Observation of large-scale traveling ionospheric disturbances of
540   auroral origin by global GPS networks/. Earth, Planets and Space **52** 669-674 (2000)
541   37. Hindley, N. P., Smith, N. D., Wright, C. J., Rees, D. A. S. & Mitchell, N. J. A two-
542   dimensional Stockwell transform for gravity wave analysis of AIRS measurements.
543   Atmos. Meas. Tech. **9**, 2545–2565 (2016).
544

545 **Code Availability**

546 All software used is either already publicly available, implements equations provided in the
547 Methods section directly, or only plots data.

563 **Author Contributions**

564 Administration: Wright
565 Conceptualisation: Wright, Hoffmann, Osprey
566 Data curation: Hoffmann, Bouillon, Carstens, Clerbaux, Mitchell, Randall
567 Formal analysis: Wright, Hindley, Alexander, Barlow, Mitchell, Prata, Hoffmann
568 Funding acquisition: Wright, Clerbaux
569 Investigation: All
570 Methodology: Wright, Hindley, Alexander, Barlow, Mitchell, Prata, Hoffmann
571 Software: Wright, Hindley, Alexander, Barlow, Mitchell, Prata, Hoffmann
572 Visualisation: Wright, Hindley, Alexander, Barlow, Prata, Carstens, Clerbaux
573 Writing – original draft: Wright, Hindley, Alexander, Hoffmann, Mitchell, Prata, Carstens,
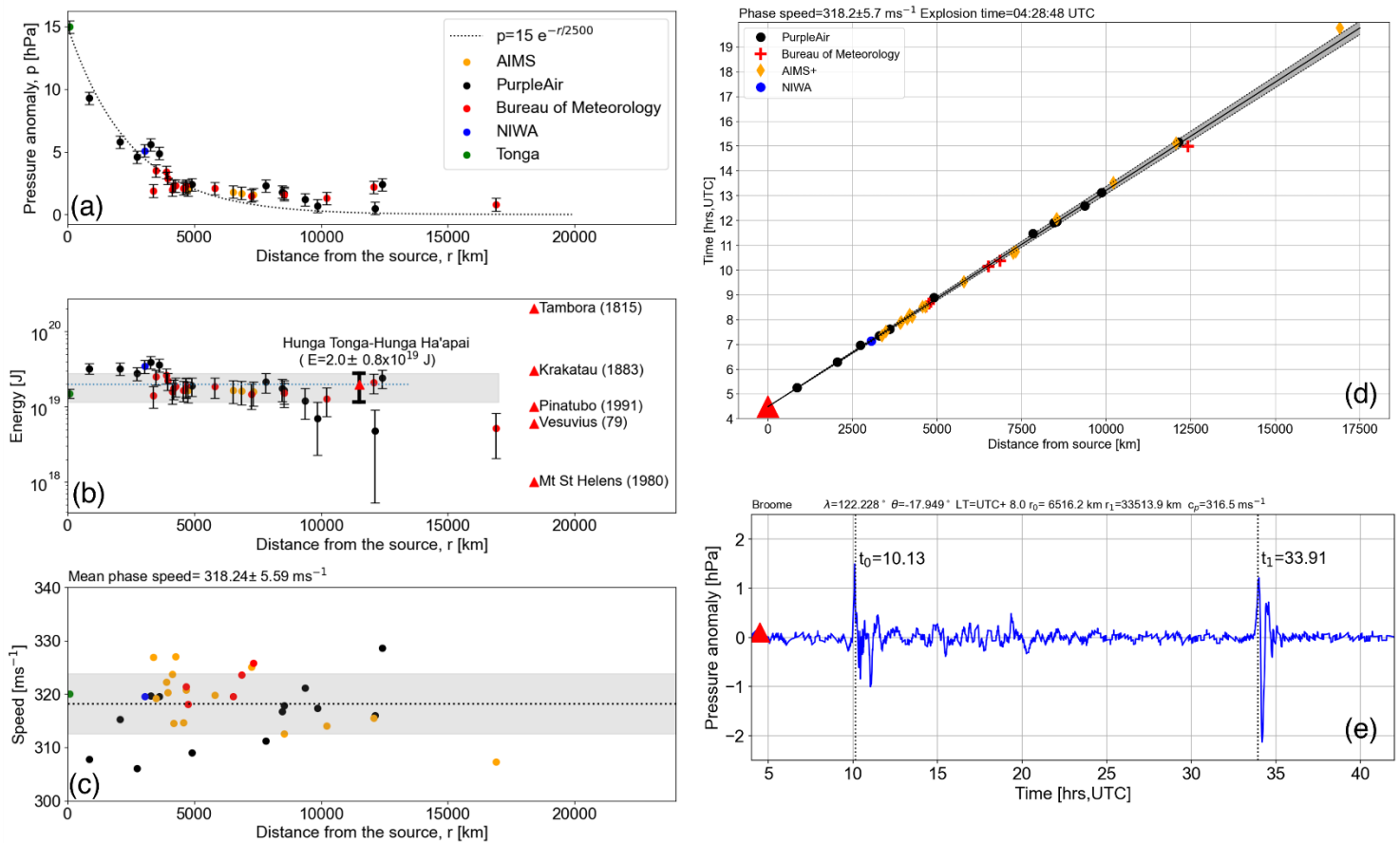574 Osprey
575 Writing - review/editing: All
576

577 **Competing Interest Declaration**

578 The authors declare no competing interests.

579 **<u>Additional Information</u>**

580 Correspondence to Corwin Wright, c.wright@bath.ac.uk.
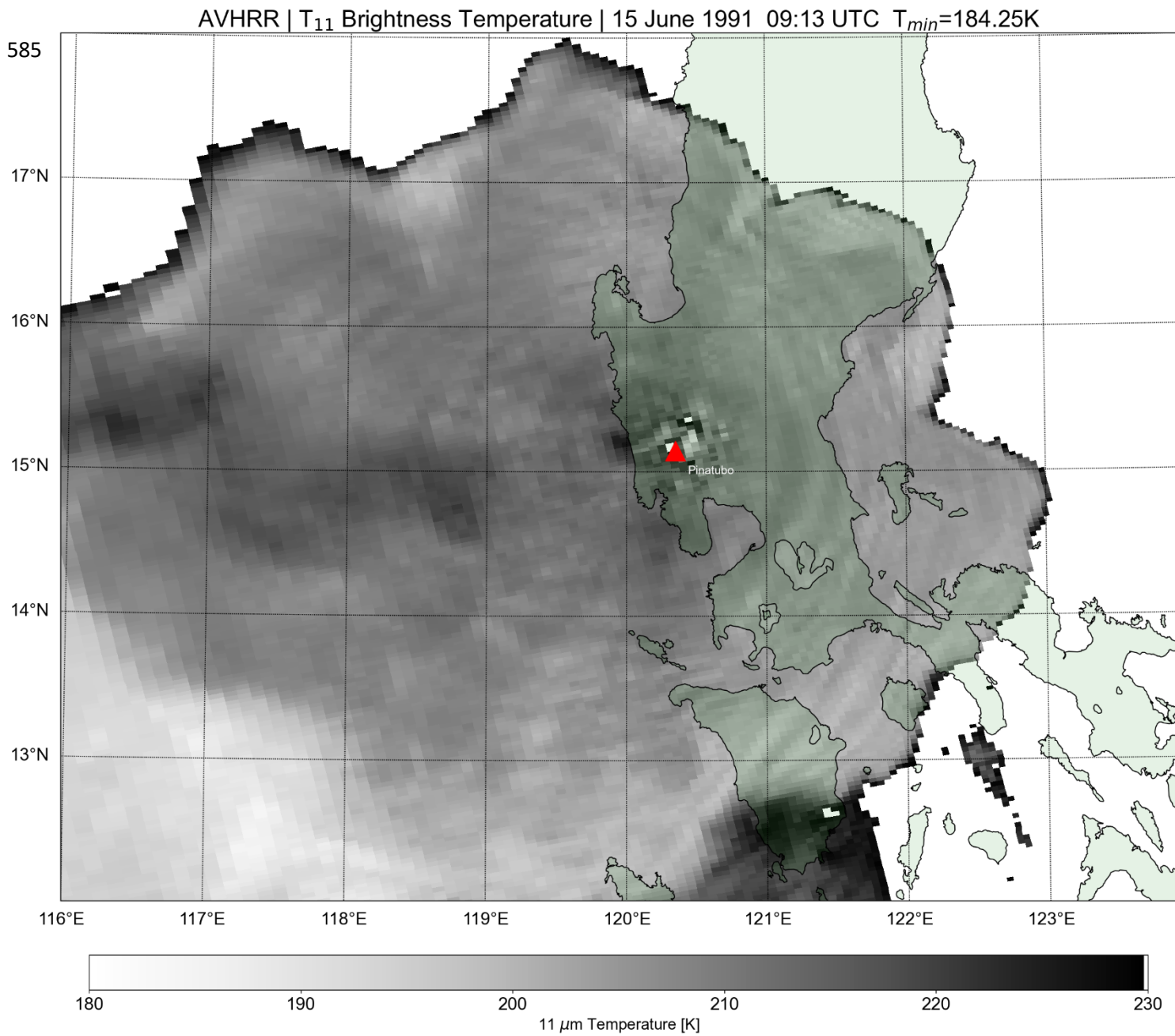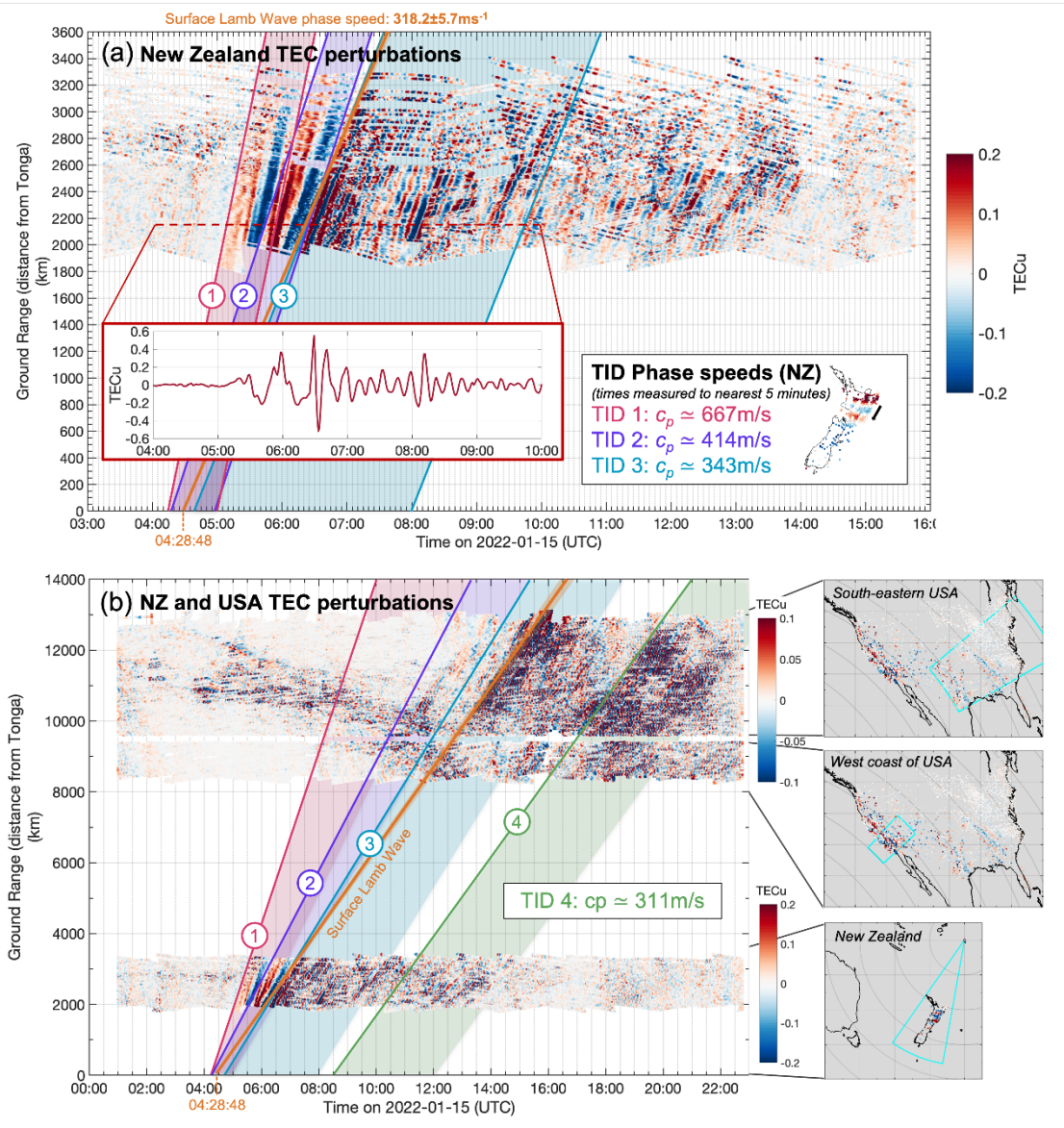
Extended Data

Extended Data Figure 1: **The eruptive energy and Lamb wave speed can be measured from surface pressure changes:** (a-d) Estimates of (a) Lamb-wave-induced pressure anomaly, (b) eruption explosive energy, (c) Lamb wave phase speed and (d) time of primary explosion, as computed from surface pressure data. (e) Time series of measured pressure anomaly at Broome, Australia. Data in all cases are derived from surface pressure stations, with the exception of reference values for other eruptions which are derived from Pyle (2000)[2]. Error bars on panels (a-b) are conservatively set to 0.5hPa.

583

584

Extended Data Figure 2: **Reprocessed data for the 1991 Pinatubo eruption shows evidence of gravity wave activity in the eruptive plume:** Brightness temperature measurements over the 1991 Pinatubo eruption plume, as observed by the Advanced Very High Resolution Radiometer. Phase fronts can be seen faintly in the cloud radiating from a point slightly west of Pinatubo.

Extended Data Figure 3: **Ionospheric data over New Zealand and North America show strong evidence of waves triggered by the Hunga Tonga eruption:** Time-distance plots of ionospheric disturbances over New Zealand and the United States, computed from GNSS-TEC data.

586
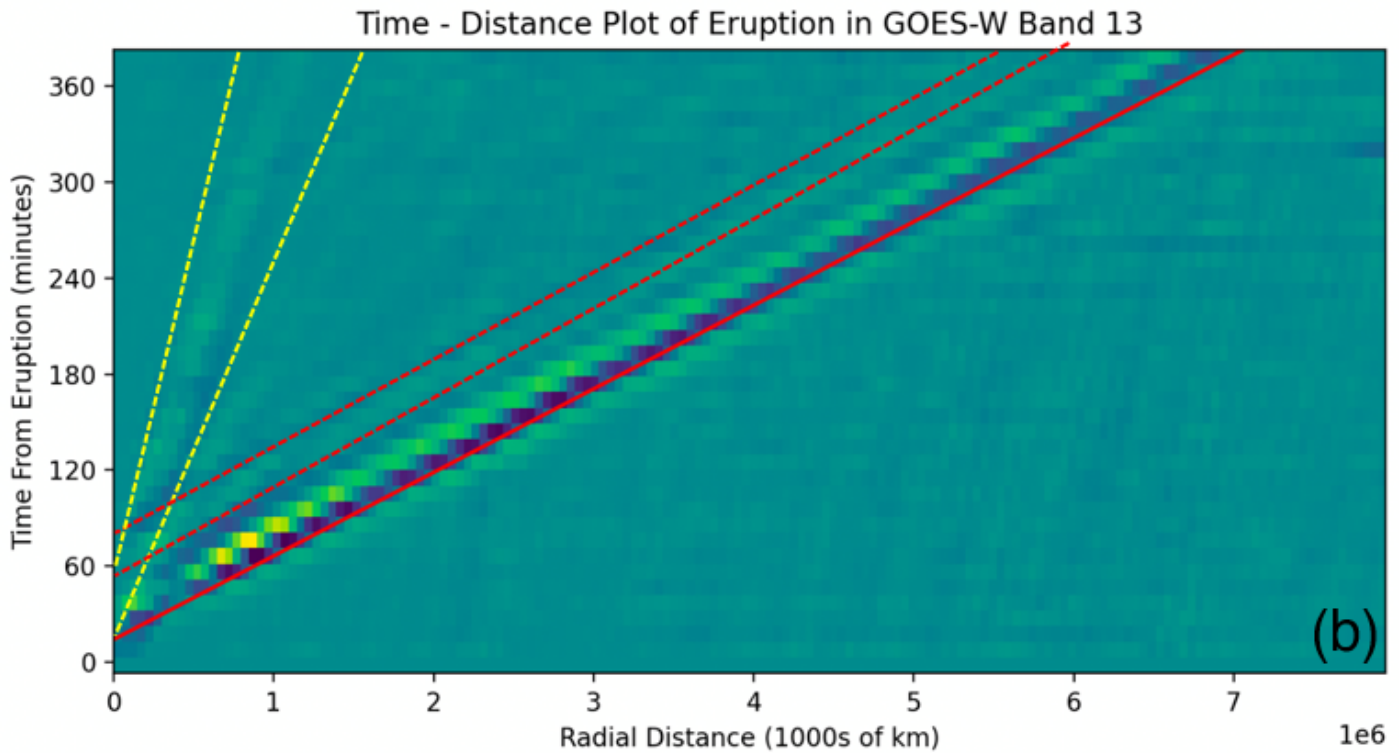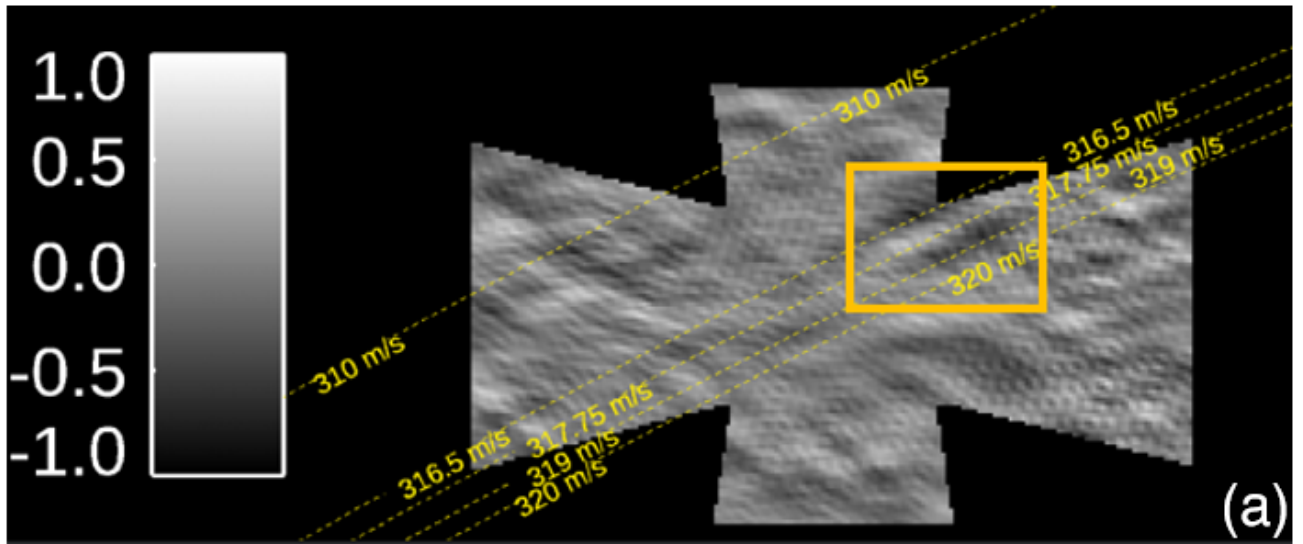
Extended Data Figure 4: **The waves generated by the eruption travelled up to the mesosphere and horizontally at speeds consistent with their types:** (a) Lamb wave as observed by CIPS (centred at 24°S 309°E, 12 300 km from Hunga Tonga, and recorded 10.75 hours after the eruption). In these data, the Lamb wave is extremely close to the instrument noise floor and statistical tests were carried out to confirm that the small signal seen is consistent with the expected speed and wavelength of the Lamb wave. (b) Time-distance spectrum derived from GOES 10um channel, with Hunga Tonga located at the origin. Red solid line identifies the primary Lamb wave, red dashed lines weaker secondary Lamb waves, and yellow dashed lines outline the limits of the dispersive gravity waves in the initially-released packet.

587
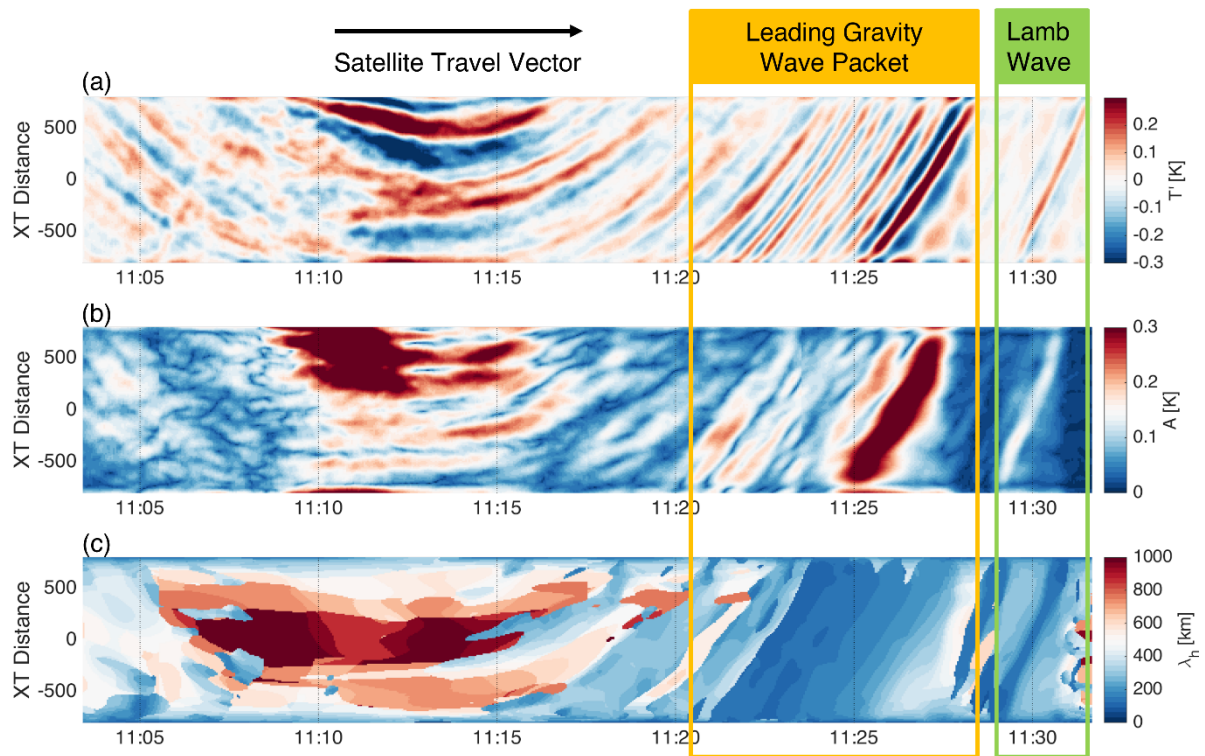
Extended Data Figure 5: **Spectral analysis provides quantitative details of stratospheric waves generated by the eruption:** 2D S-Transform[37] (2DST) estimates of gravity wave properties measured by AIRS in a descending-node pass over the Pacific Ocean on the 15th of January 2022. (a) temperature perturbations relative to a fourth-order polynomial fit across track. (b) amplitudes estimated from these perturbations using the 2DST. (c) horizontal wavelengths estimated from these perturbations using the 2DST.
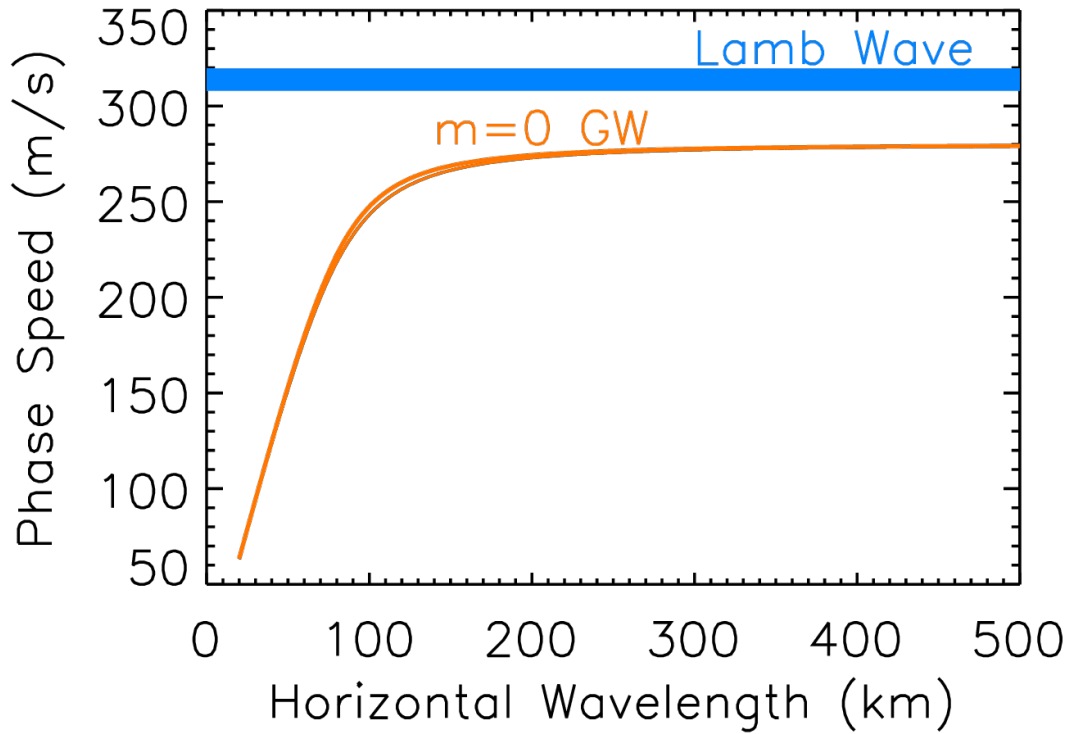
Extended Data Figure 6: **The gravity waves generated by the eruption travelled close to their maximum phase speed limit:** Expected maximum speed of a gravity wave packet relative to the observed Lamb wave, as a function of horizontal gravity wave wavelength. Blue line thickness represents the range of Lamb wave propagation speeds that we compute from AIRS, with the fast edge being approximately equal to the speed of the surface pressure signal. Orange lines represent the fast limit of gravity wave phase speeds versus horizontal wavelength, which is in the limit that the vertical wavenumber—>0. This has been calculated using the upper and lower Lamb wave speeds as the sound speed for this calculation, shown as two closely-overlaid orange lines.

589

590
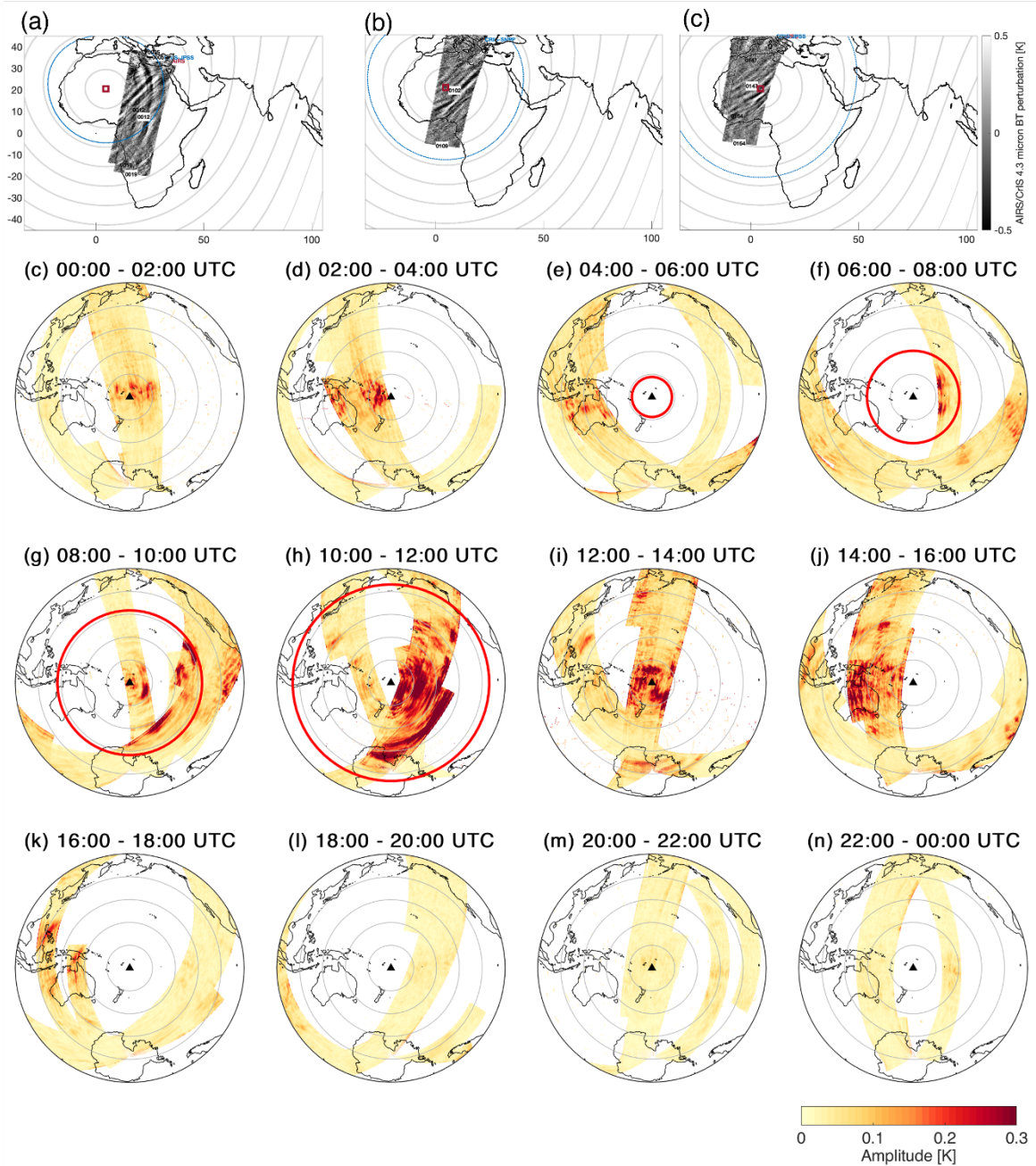
591

Extended Data Figure 7: **Gravity waves produced by the eruption traversed the entire globe and dominated the Pacific basin following the eruption:** (a-c) transit of the leading gravity wave packet over the antipode in CrIS and AIRS 4.3 μm data (d-o) GW amplitudes over Pacific computed from AIRS, IASI and CrIS 4.3 μm data using the 2DST[37].
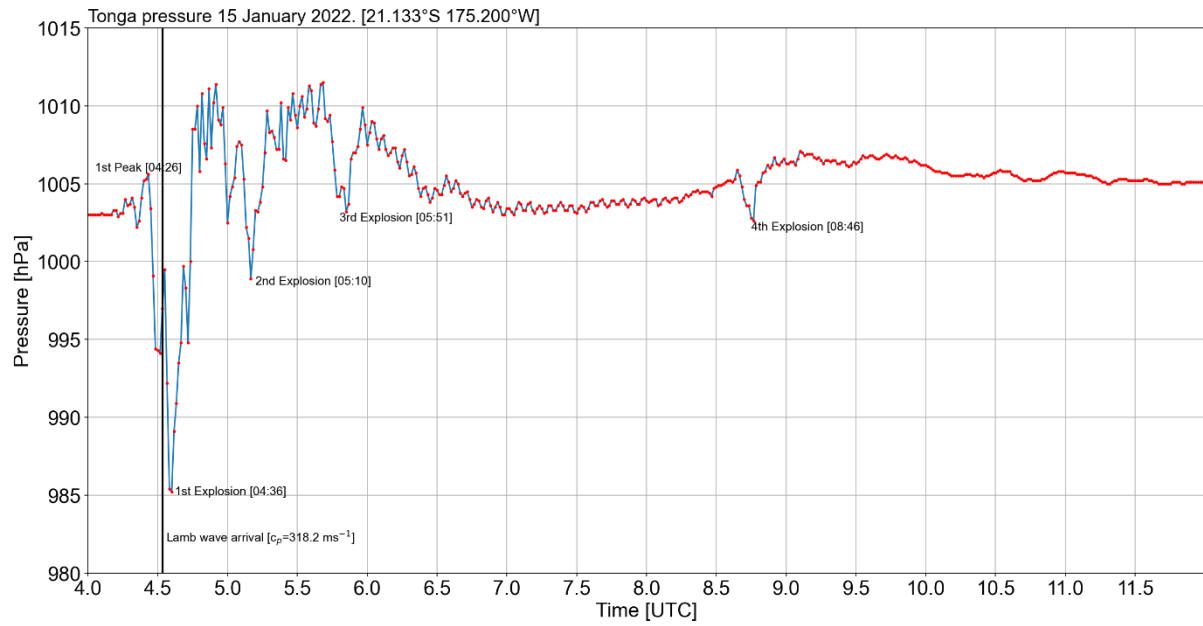
Extended Data Figure 8: **Surface pressure data shows evidence of multiple subsequent explosions:** Surface pressure station measurements from 04:00 – 12:00 UTC from Tonga, ~64km from Hunga Tonga. Note the multiple explosions after the initial primary Lamb wave trigger.
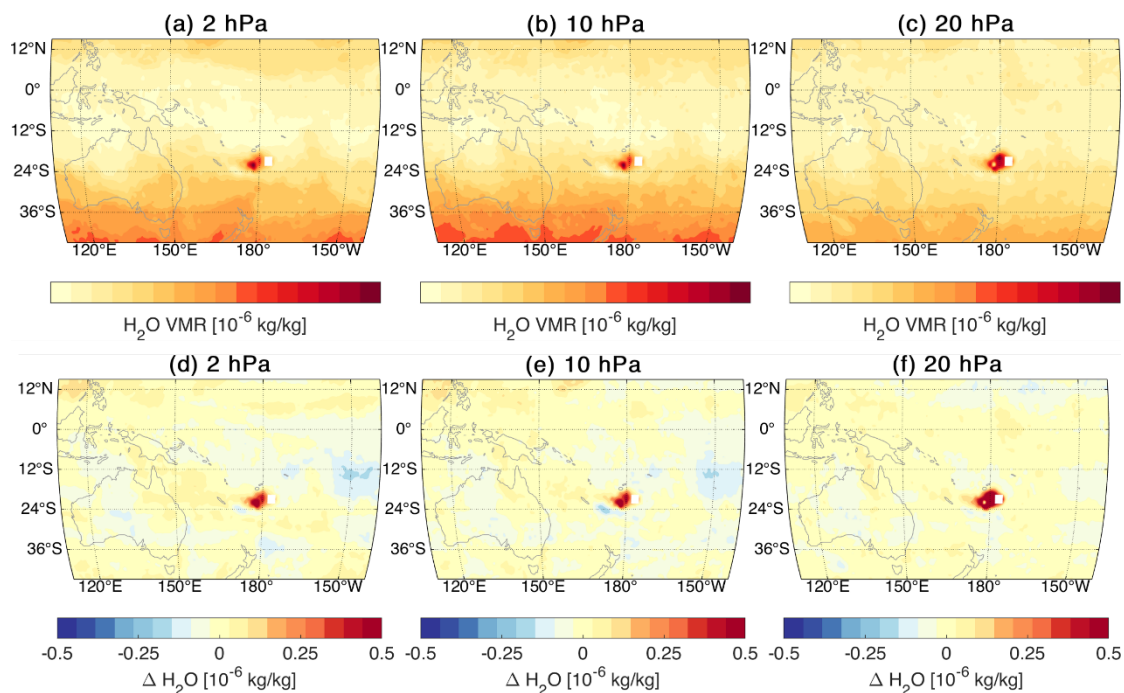
Extended Data Figure 9: **Water vapour observations are consistent with our proposed eruptive energy transfer mechanism:** 1x1 degree maps of IASI-B and IASI-C water vapour volume mixing ratio at the 2, 10 and 20hPa levels for the 15th of January 2021, using nighttime data. (a,b,c) show the data as absolute values and (d,e,f) as a difference from the local mean for January 2021. White squares indicate a lack of data due to retrieval failure, most likely due to the highly anomalous atmospheric state associated with the eruption plume.

Extended Data Figure 10: **The Lamb wave shows evidence of slowing down over South America:** Filtered data from GOES' IR channel showing the Lamb wave (strong black/white line) before (left) and after (right) passage over South America. Overlaid red line shows the the expected location of the phase front assuming uniform progression. A deviation from this expected line is seen in the portion of the wave which passed over the northern half of South America.

Supplementary Data
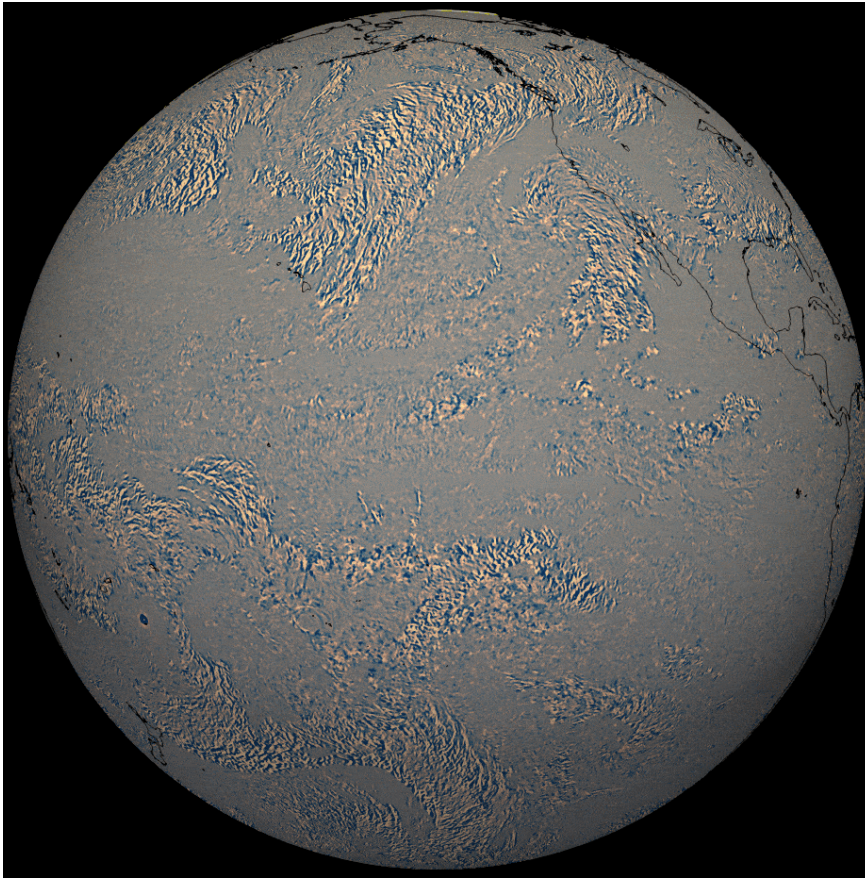
Supplementary Figure 1: GOES-derived animation of initial Lamb wave release from Hunga Tonga
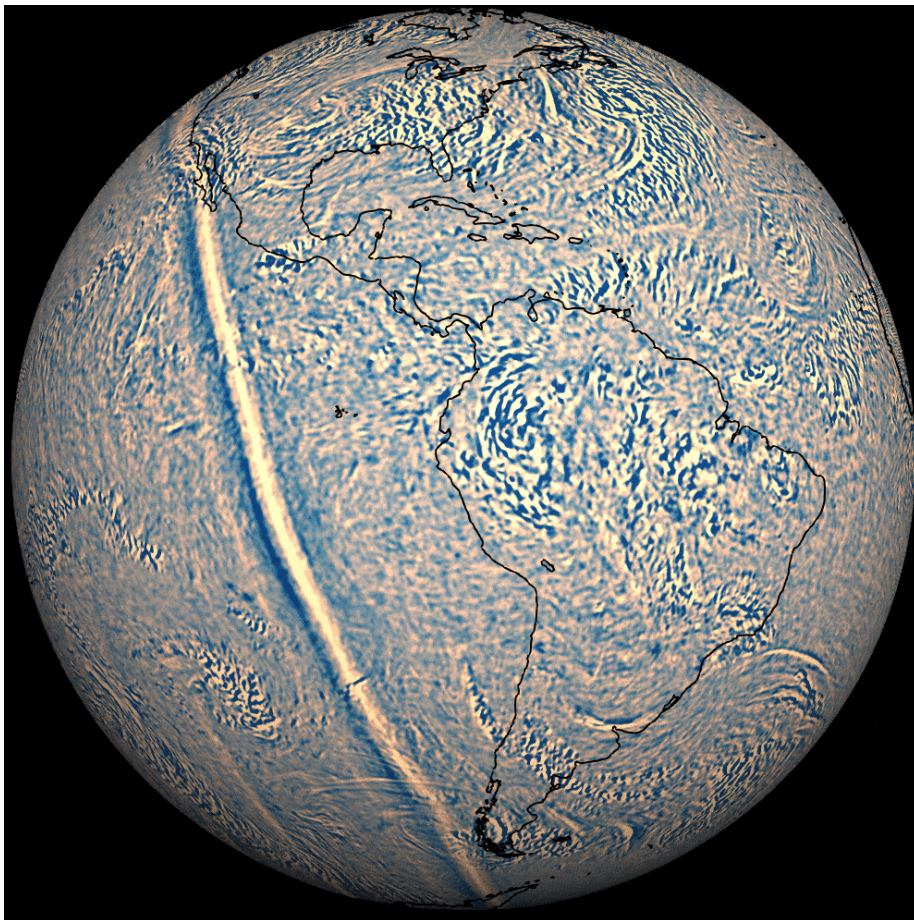
Supplementary Figure 2: GOES-derived animation showing reflection of initial Lamb wave from Hunga Tonga.

598   Supplementary Figure 3 is not included in this file due to its large filesize (>100MB), but has
599   been uploaded with the submission as an additional file.

600